

Mixed Halide Perovskites for High-Efficiency and Spectrally Stable Blue Light-Emitting Diodes

Max Karlsson

Linköping University <https://orcid.org/0000-0003-2750-552X>

Ziyue Yi

Linköping University

Sebastian Reichert

Chemnitz University of Technology <https://orcid.org/0000-0003-3214-7114>

Xiyu Luo

Linköping University

Weihua Lin

Lund University

Zeyu Lin

Beijing University of Technology

Chunxiong Bao

Linköping University <https://orcid.org/0000-0001-7076-7635>

Rui Zhang

Linköping University

Sai Bai

Linköping University <https://orcid.org/0000-0001-7623-686X>

Guanhaojie Zheng

Linköping University

Pengpeng Teng

Linköping University

Lian Duan

Tsinghua University

Yue Lu

Beijing University of Technology

Kaibo Zheng

Lund University

Tonu Pullerits

Lund University <https://orcid.org/0000-0003-1428-5564>

Carsten Deibel

Chemnitz University of Technology <https://orcid.org/0000-0002-3061-7234>

weidong xu

linköping university <https://orcid.org/0000-0002-0767-3086>

Richard Friend

University of Cambridge <https://orcid.org/0000-0001-6565-6308>

Feng Gao (✉ feng.gao@liu.se)

Linköping University <https://orcid.org/0000-0002-2582-1740>

Article

Keywords: light-emitting diodes, mixed halide perovskites, blue emission

Posted Date: December 1st, 2020

DOI: <https://doi.org/10.21203/rs.3.rs-92649/v1>

License: © ⓘ This work is licensed under a Creative Commons Attribution 4.0 International License.

[Read Full License](#)

Version of Record: A version of this preprint was published at Nature Communications on January 13th, 2021. See the published version at <https://doi.org/10.1038/s41467-020-20582-6>.

Mixed Halide Perovskites for Spectrally Stable and High-Efficiency Blue Light-Emitting

Diodes

Max Karlsson^{1,8}, Ziyue Yi^{1,2,8}, Sebastian Reichert³, Xiyu Luo^{1,4}, Weihua Lin⁵, Zeyu Zhang⁶, Chunxiong Bao¹, Rui Zhang¹, Sai Bai¹, Guanhaojie Zheng¹, Pengpeng Teng¹, Lian Duan⁴, Yue Lu⁶, Kaibo Zheng^{5,7}, Tõnu Pullerits⁵, Carsten Deibel³, Weidong Xu^{1,*}, Richard Friend², and Feng Gao^{*1}

¹Department of Physics, Chemistry and Biology (IFM), Linköping University, Linköping, Sweden.

²Cavendish Laboratory, University of Cambridge, Cambridge, UK.

³Institut für Physik, Technische Universität Chemnitz, Chemnitz, Germany.

⁴Key Lab of Organic Optoelectronics and Molecular Engineering of Ministry of Education, Department of Chemistry, Tsinghua University Beijing, China.

⁵Chemical Physics and NanoLund, Lund University, Box 124, 22100 Lund, Sweden.

⁶Institute of Microstructure and Properties of Advanced Materials, Beijing University of Technology, Beijing, China.

⁷Department of Chemistry, Technical University of Denmark, DK-2800 Kongens Lyngby, Denmark.

⁸These authors contributed equally: M. K. and Z. Y.

1 **Abstract**

2 Bright and efficient blue emission is key to further development of metal halide perovskite light-
3 emitting diodes. Although modifying bromide/chloride composition is straightforward to achieve blue
4 emission, practical implementation of this strategy has been challenging due to poor colour stability
5 and severe photoluminescence quenching. Both detrimental effects become increasingly prominent in
6 perovskites with the high chloride content that is desired to produce blue emission. Here, we solve
7 these critical challenges in mixed halide perovskites and demonstrate spectrally stable blue perovskite
8 light-emitting diodes (PeLEDs) over a wide range of emission wavelengths from 490 to 451
9 nanometres. The emission colour is directly tuned by modifying the halide composition. Particularly,
10 our blue and deep-blue PeLEDs based on three-dimensional perovskites show high EQE values of
11 11.0% and 5.5% with emission peaks at 477 and 467 nm, respectively. These achievements are enabled
12 by a vapour-assisted crystallization technique, which largely mitigates local compositional
13 heterogeneity and ion migration.

14

15 Blue light-emitting diode, with the Commission Internationale de l'Eclairage (CIE) y coordinate value
16 below 0.15 along with the $(x + y)$ value below 0.30, is of critical importance for display and energy-
17 saving lighting applications¹. Similar to preceding light-emitting technologies, achieving efficient blue
18 emission in metal halide perovskite light-emitting diodes (PeLEDs) has proven to be very challenging,
19 with performance lagging far behind their green, red and near-infrared counterparts²⁻⁷. Current efforts
20 in blue PeLEDs largely take advantage of quantum confinement effects for bandgap engineering, i.e.
21 using mixed dimensional perovskites or colloidal perovskite nanocrystals⁸⁻¹⁰. Although impressive
22 progress has been achieved in developing sky-blue PeLEDs (with CIE y > 0.15) (Supplementary Table
23 1)¹¹, there are increasing difficulties to realize blue emission using these strategies. For example, state-
24 of-the-art blue perovskite emitters achieved by strong quantum confinement commonly suffer from
25 deteriorated electronic properties due to an excess of large-size organic cations and/or over-capped
26 ligands. These issues lead to problematic charge injection and hence low brightness, as well as a big
27 gap between photoluminescence quantum yields (PLQYs) of thin films and external quantum
28 efficiencies (EQEs) of devices¹²⁻¹⁴.

29 Compared with enhancing quantum confinement, modulating the halide anions is a more
30 straightforward way to tune the bandgap of perovskites¹⁵. However, implementation of this facile
31 approach in blue PeLEDs is largely hindered by poor colour stability of the resultant blue perovskite
32 emitters (mixed bromide/chloride perovskites), due to anion segregation under electric bias¹⁶⁻¹⁸. In
33 addition, it has been widely observed that the PLQYs decrease with increasing chloride content since
34 chloride perovskites are less defect-tolerant compared to their bromide and iodide counterparts^{19,20}.
35 Both issues are particularly pronounced in perovskites with high chloride content that are desired for
36 producing blue and deep-blue emission¹⁹⁻²². Very recently, strategies on mitigating photo-induced

37 phase segregation in perovskite solar cells (*e.g.* defect passivation) have been borrowed to improve the
38 spectral stability of mixed bromide/chloride blue PeLEDs^{23,24}. These strategies were so far
39 demonstrated to be feasible only in the cases where the chloride content is low (<30%)^{22,25}.
40 Unfortunately, even by combining the strategies of mixed bromide/chloride perovskites with the
41 advantages of enhanced quantum-confinement, device performance of spectrally stable blue PeLEDs
42 is still far from practical applications (Supplementary Table 2)^{11,14,20,25}.

43 Here, we demonstrate that blue PeLEDs based on mixed-halide perovskites can be highly efficient
44 and their colour instability issues can be substantially eliminated across a large range of the blue
45 spectral region spanning 490~451 nm (with a high chloride content ranging from 30% to 57%), without
46 any assistance from enhanced quantum confinement. We show that not only halide ion migration, but
47 also compositional heterogeneity is critical for triggering phase segregation. Both factors can be
48 remarkably suppressed through depositing the perovskite films via a vapour-assisted crystallization
49 (VAC) technique. As a result, we demonstrate spectrally stable blue PeLEDs presenting a high EQE
50 value of 11.0% and a peak brightness of 2180 cd m⁻², with an emission peak at 477 nm and CIE
51 coordinates of (0.107, 0.115). In addition, we fabricate a PeLED exhibiting ideal deep-blue emission
52 at 467 nm and a decent EQE of 5.5%, which is the highest efficiency with an emission peak below 470
53 nm. The CIE coordinates of our deep-blue PeLEDs are (0.130, 0.059), approaching that of Rec. 2020
54 specified primary blue.

55 **Results and discussion**

56 **Device fabrication and spectral stability.** We prepare perovskites from precursors with a
57 stoichiometry of Cs⁺: FA⁺: Pb²⁺: [Br_{1-x}Cl_x]⁻ = 1.2: 0.3: 1: 3.5 ($x = 30\% \sim 57\%$), where FA⁺ is
58 formamidinium. In the cases of x below 20%, we do not observe any colour instability issues

59 (Supplementary Fig. 1). We focus our discussions on the perovskites from a precursor solution with x
60 = 40%, which is the most representative case due to its high chloride content, decent device
61 performance and emission within the blue region. The chloride content in this film accounts for 42%
62 of total halide anions as determined by X-ray photoelectron spectroscopy (XPS) (Supplementary Fig.
63 2). We introduce 4,7,10-trioxa-1,13-tridecanediamin (TTDDA) into the perovskite precursors as a
64 passivating agent to reduce defects⁵.

65 We show an illustration of the VAC-treatment for preparation of perovskite films in Fig. 1a. In
66 brief, the as-casted films are directly moved into a petri-dish with dimethylformamide (DMF)
67 atmosphere, followed by a typical thermal annealing process. Control samples, annealed directly after
68 spin-coating, are prepared for comparison. The different film processing techniques result in distinct
69 variations of the film morphology, i.e. a discontinuous network of large grains for the VAC-treated
70 films and full coverage of small nano-grains for the control ones, as shown in scanning electron
71 microscope (SEM) images (Supplementary Fig. 3). We observe no change in the 3D crystal structure
72 but a more preferential crystalline orientation along the (110) direction and slight enhancement of
73 crystallinity with VAC-treatment, as demonstrated by grazing incidence wide-angle X-ray scattering
74 (GIWAXS) and X-ray diffraction (XRD) measurements (Supplementary Fig. 4).

75 We fabricate the PeLEDs based on a device structure of indium tin oxide (ITO)/nickel oxide
76 (NiO_x , 10 nm)/ poly(9-vinylcarbazole) (PVK): polyvinylpyrrolidone (PVP) (10 nm)/ perovskite/
77 2,2',2''-(1,3,5-benzinetriyl)tris(1-phenyl-1H-benzimidazole) (TPBi)/ lithium fluoride (1
78 nm)/aluminium (100 nm) (Fig. 1b). The employment of NiO_x /PVK bilayer facilitates the hole injection
79 due to the cascade energy level alignment²⁶, which contributes to improve PeLED performance
80 (Supplementary Figs. 5 and 6). The PVP layer is used to improve the wettability of the precursor

81 solution on the PVK surface, as demonstrated by the reduced water contact angle after PVP deposition
82 (Supplementary Fig. 7). The high-angle annular dark-field scanning transmission electron microscope
83 (HAADF-STEM) and energy-dispersive X-ray spectroscopy (EDX) device cross-sectional images
84 indicate higher TPBi layer thickness (~ 50 nm) on the bottom hole injection layer with respect to that
85 on perovskite grains (~ 35 nm) (Fig. 1b and Supplementary Fig. 8 (carbon distribution)), leading to
86 enhanced local resistance at the TPBi/PVK:PVP interface. Combined with the large injection barrier
87 caused by the energy level mismatch between TPBi and PVK, the discontinuous morphology in VAC-
88 treated devices does not necessarily lead to strong electrical shunts under normal PeLED operational
89 conditions^{3,5} (Supplementary Fig. 9). Notably, the VAC-treated devices with varying chloride content
90 (30~40%) show considerable enhancement of EQE values compared to the respective control samples
91 (Fig. 1c). We show the characteristics of the representative devices in Supplementary Fig. 10. We
92 notice that, as expected, our device performance also benefits from the efficient defect passivation
93 ability of TTDDA (Supplementary Fig. 11).

94 The VAC-treated devices show stable electroluminescence (EL) with a negligible shift of the CIE
95 coordinates up to ~ 400 mA cm⁻² (6~6.5 V), which is far above maximum light output (L_{\max}) conditions
96 at 100 mA cm⁻²/5.0 V (Fig. 1d). The EL spectrum obtained at a high voltage (or current density) of 6
97 V (~ 400 mA cm⁻²) is only slightly broader than that at 3.5 V (~ 3 mA cm⁻²) (Fig. 1e). We attribute this
98 slight EL broadening to charge carrier/phonon interaction due to Joule heating²⁷, as similar behaviour
99 is observed in pure-bromide PeLEDs (Supplementary Fig. 12). In contrast, the control devices undergo
100 distinct emission colour changes starting at very low bias and current density of around 3.0~3.5 V and
101 1~5 mA cm⁻² (Figs. 1d and e), analogous to previous reports on spectrally unstable mixed
102 bromide/chloride PeLEDs^{16,21}. Under the harsh operational condition, that is, with the bias larger than

103 6.5 V, distinct colour change is observable even in VAC-treated devices. We emphasize that in this
104 case the current density is over 400 mA cm^{-2} , which is far above normal working conditions of reported
105 blue PeLEDs^{11,14,20,25}. Notably, we observe abnormal plateau-like J - V characteristics during the voltage
106 sweep at 6~6.5 V and severe PL quenching after the operation (Supplementary Fig. 13), indicating
107 severe device damage due to perovskite and/or interfacial degradation. Given the high current density,
108 Joule heating could be a critical reason²⁸.

109 With VAC-treatment, we demonstrate spectrally stable PeLEDs with emission colours from sky-
110 blue to deep-blue (emission peaks at 490 to 451 nm) by simply varying the chloride content (30%~57%)
111 (Fig. 1f and Supplementary Fig. 14). We also examine the spectral stability of our devices at a constant
112 current density of 5 mA cm^{-2} (with initial luminance ranging from ~ 200 to $\sim 600 \text{ cd m}^{-2}$ for different
113 devices). Although the operational lifetime is no better than those in previously reported blue PeLEDs
114 (with T_{50} around 1~2 min)^{8,11,12,20}, we observe no spectral shift even after 10 minutes of operation
115 (Supplementary Fig. 15). Previous reports on photoinduced phase segregation in mixed halide
116 perovskites indicate that it is only triggered when the excitation density is above a certain threshold,
117 below which little to no effects are present^{29,30}. Our results are consistent with these observations,
118 indicating that employing mixed halide anions is a feasible approach for blue PeLEDs as long as we
119 can control the phase segregation threshold to be far above working conditions.

120 **The origin of improved spectral stability.** Although the underlying reason for phase segregation is
121 complicated, previous investigations on perovskite solar cells propose that three factors may be
122 collectively contributing to this phenomenon. These three factors include a polaron induced strain
123 effect³¹, a thermodynamic process as driven by free energy differences associated with composition

124 and band offsets³², and field-dependent anion motion³³. We carry out a series of characterizations to
125 understand the origin of the spectral stability of PeLEDs based on VAC-treated perovskite films.

126 We first measure PL properties of our perovskite films. We observe obviously enhanced PLQYs
127 in the VAC-treated films across a wide range of excitation fluences, with a peak PLQY of 12%
128 compared to 3% for the control sample (Fig. 2a). Time correlated single photon counting (TCSPC)
129 measurements demonstrate a prolonged PL lifetime for VAC-treated samples compared to the control
130 one (Fig. 2b). These results suggest fewer defects and much suppressed non-radiative recombination
131 in the VAC-treated films, consistent with the higher EQEs of the devices. We believe that the enhanced
132 spectral stability in our PeLEDs is partially ascribed to the reduced defects, as defects are generally
133 believed to act as channels for anion hopping and hence facilitate phase segregation³⁴.

134 In addition to the reduced defect density, we also observe significantly improved local
135 compositional homogeneity in the VAC-treated films compared to the control sample. It is first
136 evidenced by a steeper edge of the absorption spectrum (Supplementary Fig. 16a) and a much-
137 narrowed PL linewidth (with full-width at half-maximum (FWHM) of ~18 nm) of VAC-treated films
138 compared to that of control samples (FWHM of ~25 nm) (Fig. 2c). To gain further understanding of
139 electronic states in the films, we conducted transient absorption (TA) spectroscopy measurements. The
140 control film displays a broad photobleaching peak that shifts from 455 nm to 465 nm (Fig. 2d and
141 Supplementary Figs. 16b-c), which is consistent with the coexistence of different phases. As there is
142 no sign of low-dimensional phases from GIWAXS and XRD patterns, we assign the compositional
143 heterogeneity in the control films to a non-uniform distribution of halide anions, which has been widely
144 reported in bromide/iodide mixed perovskites^{35,36}. In contrast, the VAC-treated film shows a single

145 narrow ground state photobleaching situated at 473 nm, indicating a high compositional homogeneity.
146 According to current polaronic and thermodynamic models for rationalizing phase segregation in
147 perovskite solar cells, a high compositional heterogeneity can contribute to the phase
148 segregation^{31,32,37-39}. In specific, fluctuations in halide compositions can yield heterogeneous regions
149 in the perovskites where polarons tend to localize at lower bandgap areas, leading to enhanced local
150 lattice strain which drives de-mixing of halide anions^{31,38,39}. A system with initially high free energy
151 due to severe compositional disorder might be energetically unfavourable for phase stability as
152 indicated by the thermodynamic model³⁷. Lattice mismatch and discrepancy of band offsets between
153 different phases are also believed to be the driving forces for phase segregation^{32,37}. Our observations
154 are in line with these previous investigations, demonstrating the critical role of high homogeneity in
155 improving phase stability of VAC-treated devices.

156 Assured about the reduced defects and improved compositional homogeneity in VAC-treated
157 films, we then evaluate field-dependent ion migration in our devices. We perform temperature-
158 dependent admittance spectroscopy, from which we can determine ion migration activation energy
159 (E_A), ion diffusion coefficient (D), and concentration of mobile ions (N_i)⁴⁰. The capacitance (C)
160 response of mobile ionic species can be probed by varying the frequency (ω) of an applied alternating
161 voltage and the temperature. We show the admittance spectra in Supplementary Fig. 17 and the plots
162 of derivations ($-\omega dC/d\omega$ versus ω) in Figs. 2e and 2f. Two distinct signatures from mobile ionic species
163 are visible, which are labelled ϵ and β . We confirm that the charge transport layers are not responsible
164 for these signatures by characterizing devices with only charge transport layers (Supplementary Fig.
165 18)⁴¹. In particular, we observe that the response peaks at the low-frequency region (ϵ) in the VAC-
166 treated devices are much less prominent than those in the control devices, suggesting a much lower

167 mobile ion concentration. We show the deduced Arrhenius plots in Supplementary Fig. 19 and
168 summarize all the obtained parameters (E_A , D , and N_i) in Supplementary Table 3. The E_A values of ion
169 diffusion for both ϵ and β are very close in the two samples, implying that the mode of ion migration
170 is not significantly altered. Both the concentration of mobile ions and ion diffusion coefficient are
171 reduced in VAC-treated devices compared to the control devices. The most striking difference occurs
172 to $N_i(\epsilon)$, which is decreased from $5.4 \times 10^{16} \text{ cm}^{-3}$ to $1.6 \times 10^{16} \text{ cm}^{-3}$. Considering the small E_A of ϵ (~ 0.2
173 eV), we assign them to mobile halide anions^{33,40}. The mitigated halide migration can be a result of
174 reduced ionic defects, as confirmed by PLQYs and TCSPC results³⁴.

175 Based on the analysis above, we conclude that the excellent spectral stability in VAC-treated
176 devices originates from a synergistic effect of less ionic defects, mitigated ion migration and a higher
177 compositional homogeneity.

178 **Understanding the effect of the VAC-treatment process.** Having understood the origin of high
179 colour stability and excellent device performance, the question that remains is how VAC-treatment
180 brings about these effects. We conduct SEM measurements to track the grain growth and
181 morphological evolution of the films during the VAC treatment. We clearly observe two stages. The
182 first stage happens within the first minute of vapour treatment, showing a crystal growth from initially
183 formed small grains into large ones, accompanied by the morphological evolution from dense films
184 into discontinuous network (Supplementary Fig. 20). Considering the presence of crystalline
185 perovskites within the pristine films and the diffusive vapour atmosphere, we assign the process of
186 grain growth to Ostwald ripening. The wet films preserved by DMF vapour can be regarded as a sol
187 system, with the solvent as the dispersing medium and perovskites as the dispersed phases. The
188 ripening process occurs because large grains are more energetically favoured to smaller grains, leading

189 to reduced grain boundaries and hence fewer defects. The second stage happens during the prolonged
190 duration of treatment, which only has a slight impact on the morphology.

191 We also employ in-situ PL and transmittance measurements to monitor the crystal growth with
192 and without DMF vapour. The measurement setups are illustrated in Supplementary Fig. 21. Initially,
193 both films show broad emission bands with the main peak at the low-energy region and a
194 distinguishable shoulder at the high-energy region, which are labelled as P1 and P2, respectively (Figs.
195 3a and 3b). We speculate that the high-energy emission originates from initially formed Cl-rich
196 perovskite phases due to their fast nucleation and crystallization, as governed by their poor solubility
197 compared to Br-rich counterparts. By following the PL spectral evolution with time, we observe a
198 gradual disappearance of P2 and a continuous red-shift of P1 in VAC-treated samples, leading to a
199 narrow and single-emission peak eventually (Fig. 3b). To further clarify the spectral evolution of VAC-
200 treated films in different time scales, we show the changes of emission bandwidth as well as the
201 proportion of P2 (A_{P2}) to a total area of emission band (A) with time in Fig. 3c. We find that the most
202 striking changes occur within the first five minutes of treatment, while prolonged duration of up to 20
203 minutes results in only a small difference (Fig. 3c). This PL evolution is consistent with the results of
204 in-situ transmittance measurements, i.e. a red-shift of absorption onset and steeper absorption edge
205 after VAC-treatment (Supplementary Fig. 22a). In contrast, keeping the pristine films in the glovebox
206 atmosphere does not change the PL (Fig. 3a) and transmittance (Supplementary Fig. 22b) spectra to
207 any significant degree over time.

208 Based on the in-situ spectroscopic measurement results, we can now rationalize the effect of the
209 VAC-treatment. It provides a favourable diffusive environment for halide rearrangement within the
210 films (Fig. 3d), which undergo an equilibrating crystallization process that homogenises local chemical

211 composition and reduces disorder. Initially, the as-casted films are composed of various Cl-rich solid
212 phases and Br-rich components in liquid phases due to nonequilibrium grain growth during spin-
213 casting. For the films with no vapour atmosphere, quick solvent evaporation and following fast
214 crystallization result in immediate freezing of the perovskite composition. The post-annealing could
215 mitigate phase heterogeneity to some extent, as indicated by the weakened emission shoulder at short
216 wavelength (P2) after annealing (Fig. 2c). However, the initially formed heterogeneous phases are still
217 partially preserved in the resulting films. In contrast, with the presence of DMF vapour, the liquid
218 phase can be preserved for a long duration. This facilitates and prolongs the following halide exchange
219 process as driven and modulated by the chemical potential difference between solid (Cl-rich) and
220 liquid phases (Br-rich), resulting in a rearranged composition that gradually approaches chemical
221 equilibrium and homogeneous distribution of constituents. The following annealing procedure has
222 little impact on the PL spectra of VAC-treated films, further confirming that the high homogeneous
223 composition has already been achieved during the VAC-treatment.

224 We then tune the duration of DMF vapour-treatment to assess the impact on spectral stability and
225 device efficiency in different timescale (Fig. 3e and 3f), further supporting our understanding of this
226 technique. We observe distinct batch to batch variations in EL spectra and dispersion of CIE
227 coordinates in control devices (Fig. 3e and Supplementary Fig. 23a), ascribed to nonequilibrium crystal
228 growth and hence uncontrollable local film composition. In contrast, EL spectra and CIE coordinates
229 of VAC-treated devices are highly reproducible between batches, resulting from self-moderated halide
230 rearrangement during the VAC-treatment (Fig. 3e and Supplementary Fig. 23b). When comparing the
231 devices processed with different duration of VAC treatment, we observe a remarkable EQE
232 enhancement in one minute of treatment, that is, with averaged peak EQE values improved from $\sim 0.6\%$

233 to ~3.8% (Fig. 3f), which well corresponds to the dramatical morphological variations in the same time
234 scale from SEM results (Supplementary Fig. 20). We believe that perovskite re-crystallization,
235 enlarged grain size and improved local homogeneity collectively help to reduce the defect density and
236 hence reduce non-radiative recombination. In addition, the isolated nano-structures may also
237 contribute to the efficiency improvement due to enhanced light-out coupling³. With increasing the
238 processing duration, the EQE values gradually approach saturation. We assign this to a slow diffusion-
239 mediated defect healing process from the gradually improved homogeneity that reduces local lattice
240 mismatch and strain-induced interfacial defects^{42,43}. Notably, one minute of VAC-treatment is
241 sufficient for improving the efficiency but not the spectral stability (Fig. 3e), indicating that
242 discontinuous morphology has little impact on improving phase stability. In other words, a large
243 perovskite grain with size scale of hundreds of nanometres in our samples can hardly be the reason for
244 the suppression of phase segregation within the grain, as probed in previous reports showing that the
245 phase segregated domain can be as small as ~8 nm^{30,32}. We also notice that the devices with five-
246 minute treatment show comparable colour stability to those with twenty-minute treatment (Fig. 3e),
247 corresponding well to the time scale of the disappearance of high energy phases as observed in Fig.
248 3c. It further confirms the critical role of high compositional homogeneity in improving phase stability.

249 Given the critical role of diffusive environment on retarding crystallization for halide
250 rearrangement, a proper solubility of perovskite precursors in the solvent vapour might be the key to
251 achieving high compositional homogeneity. We thus perform additional experiments using dimethyl
252 sulfoxide (DMSO) or chloroform as the alternative vapour for further understanding the VAC
253 treatment. DMSO is another commonly used solvent for perovskite precursors, while chloroform is a
254 well-known “anti-solvent” that is widely used to accelerate perovskite crystallization⁴⁴. Considering

255 that the vapour residues in the glovebox may affect the results, we also prepare the samples without
256 introducing any vapour on purpose, that is, leaving the as-casted films in the glovebox for the same
257 duration. As shown in Supplementary Fig. 24, the introduction of chloroform vapour has no positive
258 effect on either device efficiency or spectral stability, which can be attributed to the poor solubility of
259 perovskite precursors in chloroform, leading to a fast crystallization and freezing of the composition,
260 and hence resulting in high heterogeneity. In contrast, DMSO treatment gives comparable
261 improvement as DMF vapour, further rationalising our understanding of the effect of the vapour
262 treatment.

263 **The general applicability of VAC-treatment and device optimization.** We proceed to explore the
264 VAC-treatment in other material systems, aiming to further improve the device performance and
265 validate the general applicability. We incorporate a small amount of rubidium ions (Rb^+) in our
266 perovskites, that is, using a precursor composition of $\text{Rb}^+ : \text{Cs}^+ : \text{FA}^+ : \text{Pb}^{2+} : [\text{Br}_{0.6}\text{Cl}_{0.4}]^- = 0.1 : 1.2 : 0.2 :$
267 $1 : 3.5$. Consistent with the previous reports in perovskite solar cells^{45,46}, the incorporation of Rb^+
268 effectively suppresses non-radiative recombination as indicated by a considerable enhancement of
269 peak external PLQY (25%) and a prolonged PL lifetime (Supplementary Figs. 25a and b). The small
270 amount of Rb^+ addition has little impact on the film morphology (Supplementary Fig. 25c).

271 We show the characteristics of the best-performing VAC-treated Rb-device using 40% Cl content
272 in Fig. 4. The device exhibits blue emission peaking at 477 nm with FWHM of 18 nm. The
273 corresponding CIE coordinates are (0.107, 0.115), approaching the primary blue (0.14, 0.08) specified
274 by the National Television System Committee (NTSC). Compared to the device without using VAC-
275 treatment (Supplementary Fig. 26), the treated device shows a significant enhancement of EQE value
276 up to 11.0%. The luminance rises rapidly after the device turns on at a low voltage of 2.6 V, reaching

277 a peak value of 2,180 cd cm⁻² at 5.0 V (106 mA cm⁻²). The low turn-on voltage and high brightness
278 indicate efficient charge injection, which is usually very challenging in strongly confined perovskites¹⁴.
279 We observe no peak shift during voltage scans until reaching a high bias at 6.0 V (~300 mA cm⁻²)
280 (Supplementary Fig. 27a), analogous to the device without Rb⁺ incorporation, further indicating that
281 phase segregation in VAC-treated devices is mainly mediated by the device damage at harsh operating
282 conditions. In addition, we demonstrate that no EL shift can be observed even after 75 min of operation
283 at 3 V (~0.1 mA cm⁻², with initial luminance of ~10 cd m²) (Supplementary Fig. 27b). Although Rb⁺
284 addition significantly improves the device efficiency, we have not observed any distinct effect on
285 operational stability (~3 min, Supplementary Fig. 27c and d). The short operational lifetime could be
286 a result of Joule heating and ion-migration induced material and/or interfacial degradation under the
287 bias^{9,28}, as well as Al diffusion and relevant redox reaction between Pb²⁺ and Al⁰⁴⁷. An EQE histogram
288 for 40 devices shows an average peak EQE of 9.3% with a low standard deviation of 0.67%, indicating
289 high reproducibility of the VAC-treatment.

290 Further increasing Cl content to 45% results in deep-blue emission, whose device characteristics
291 are also summarized in Fig. 4. The corresponding CIE coordinates are (0.130, 0.059), very close to
292 Rec. 2020 specified blue standards (0.131, 0.046). The deep-blue PeLEDs achieves a peak EQE of
293 5.5% and an average peak EQE of 3.9% with a standard deviation of 0.76%, which are among the best
294 for PeLEDs with ideal deep-blue emission.

295 We demonstrate that the VAC-treatment is also applicable for improving the colour stability and
296 device performance of low-dimensional perovskites with mixed bromide/chloride anions, e.g. the
297 typical phenethylammonium (PEA⁺)-modified CsPb(Br_{0.7}Cl_{0.3})₃ (Supplementary Fig. 28). These
298 results indicate that the wavelength of the previously reported high-performance sky-blue PeLEDs

299 based on quasi-2D perovskites could be pushed to a bluer region without any negative impacts on their
300 colour stability and device efficiency.

301 **Conclusion**

302 In summary, we have demonstrated that the notorious colour instability issues in mixed halide blue
303 PeLEDs can be substantially mitigated across a wide range of emission colour from sky blue to deep
304 blue region (490 to 451 nm). The excellent phase stability is mainly achieved by the development of a
305 vapour-assisted crystallization technique that effectively suppresses the ion migration and
306 compositional heterogeneity. Particularly, for the first time, we show high-efficiency and spectrally
307 stable blue and deep-blue PeLEDs based on mixed halide 3D perovskites, with respective peak EQEs
308 of 11.0% and 5.5%, presenting two of the most efficient blue PeLEDs to date. Our findings are also
309 applicable to the prevailing low-dimensional blue perovskite emitters, indicating a bright future for
310 further improvement of blue PeLEDs by combining these two strategies. Our research thus provides a
311 broad avenue for future development of blue perovskite emitters, representing another milestone
312 towards practical implementation of perovskite light-emitting diodes in full-colour displays and
313 lighting applications. Beyond that, stabilized mixed halide perovskites are also of great interest for a
314 wide range of perovskite applications where the bandgap needs to be finely controlled, for instance,
315 lasing and tandem solar cells.

316 **Acknowledgement**

317 We thank D. Egger, X. Zhu, C. Yin, H. Tian and J. Li for valuable discussions, and X. Liu for help
318 with the XPS measurements. We acknowledge the support from the ERC Starting Grant (No. 717026),
319 the Swedish Energy Agency Energimyndigheten (No. 48758-1 and 44651-1), Swedish Research

320 Council VR, NanoLund and the Swedish Government Strategic Research Area in Materials Science
321 on Functional Materials at Linköping University (Faculty Grant SFO-Mat-LiU No. 2009-00971). C.D.
322 and S.R. acknowledge financial support by the Bundesministerium für Bildung und Forschung (BMBF
323 Hyper project, contract no. 03SF0514C) and the DFG (no. DE 830/22-1) within the framework of SPP
324 2196 programme. Y. L. acknowledge financial support from the National Key Research and
325 Development Program of China (2016YFB0700700), the National Natural Science Foundation of
326 China (11704015, 51621003, 12074016), the Scientific Research Key Program of Beijing Municipal
327 Commission of Education, China (KZ201310005002), and the Beijing Innovation Team Building
328 Program, China (IDHT20190503). F.G. is a Wallenberg Academy Fellow.

329 **Author Contributions**

330 F.G. and W.X. conceived the idea and supervised the project; M.K. performed the experiments and
331 analysed the data; Z.Y. developed Rb-doped devices and low-dimensional perovskite-based devices;
332 R.S. performed admittance spectroscopy and analysed the data under the supervision of C.D.; X.L.
333 and P.T. contributed to device fabrication and measurements; W.L. performed transient absorption
334 under the supervision of K.Z. and T.P.; Z.L. performed transmission electron microscopy under the
335 supervision of Y.L.; R. Z. and G. Z. performed GIWAXS measurements and analysed the data; C.B.,
336 S.B., L.D. and R.F. contributed the interpretation of results; M.K., W.X. and F.G. wrote the manuscript;
337 S.B. provided revisions to the manuscript; All authors discussed the results and commented on the
338 manuscript.

339 **Additional information**

340 Supplementary information is available in the online version of the paper. Correspondence to W. X.
341 and F.G.

342 **Data availability**

343 The data that support the plots within this paper and other findings of this study are available from the
344 corresponding author upon reasonable request.

345 **Competing interests**

346 The authors declare no competing interests.

347 **Reference**

- 348 1. Zhu, M. & Yang, C. Blue fluorescent emitters: Design tactics and applications in organic light-
349 emitting diodes. *Chem. Soc. Rev.* **42**, 4963-4976 (2013).
- 350 2. Tan, Z. K. *et al.* Bright light-emitting diodes based on organometal halide perovskite. *Nat.*
351 *Nanotechnol.* **9**, 687-692 (2014).
- 352 3. Cao, Y. *et al.* Perovskite light-emitting diodes based on spontaneously formed submicrometre-
353 scale structures. *Nature* **562**, 249-253 (2018).
- 354 4. Lin, K. *et al.* Perovskite light-emitting diodes with external quantum efficiency exceeding 20 per
355 cent. *Nature* **562**, 245-248 (2018).
- 356 5. Xu, W. *et al.* Rational molecular passivation for high-performance perovskite light-emitting
357 diodes. *Nat. Photon.* **13**, 418-424 (2019).
- 358 6. Chiba, T. *et al.* Anion-exchange red perovskite quantum dots with ammonium iodine salts for
359 highly efficient light-emitting devices. *Nat. Photon.* **12**, 681-687 (2018).
- 360 7. Zhao, B. *et al.* High-efficiency perovskite–polymer bulk heterostructure light-emitting diodes.
361 *Nat. Photon.* **12**, 783-789 (2018).

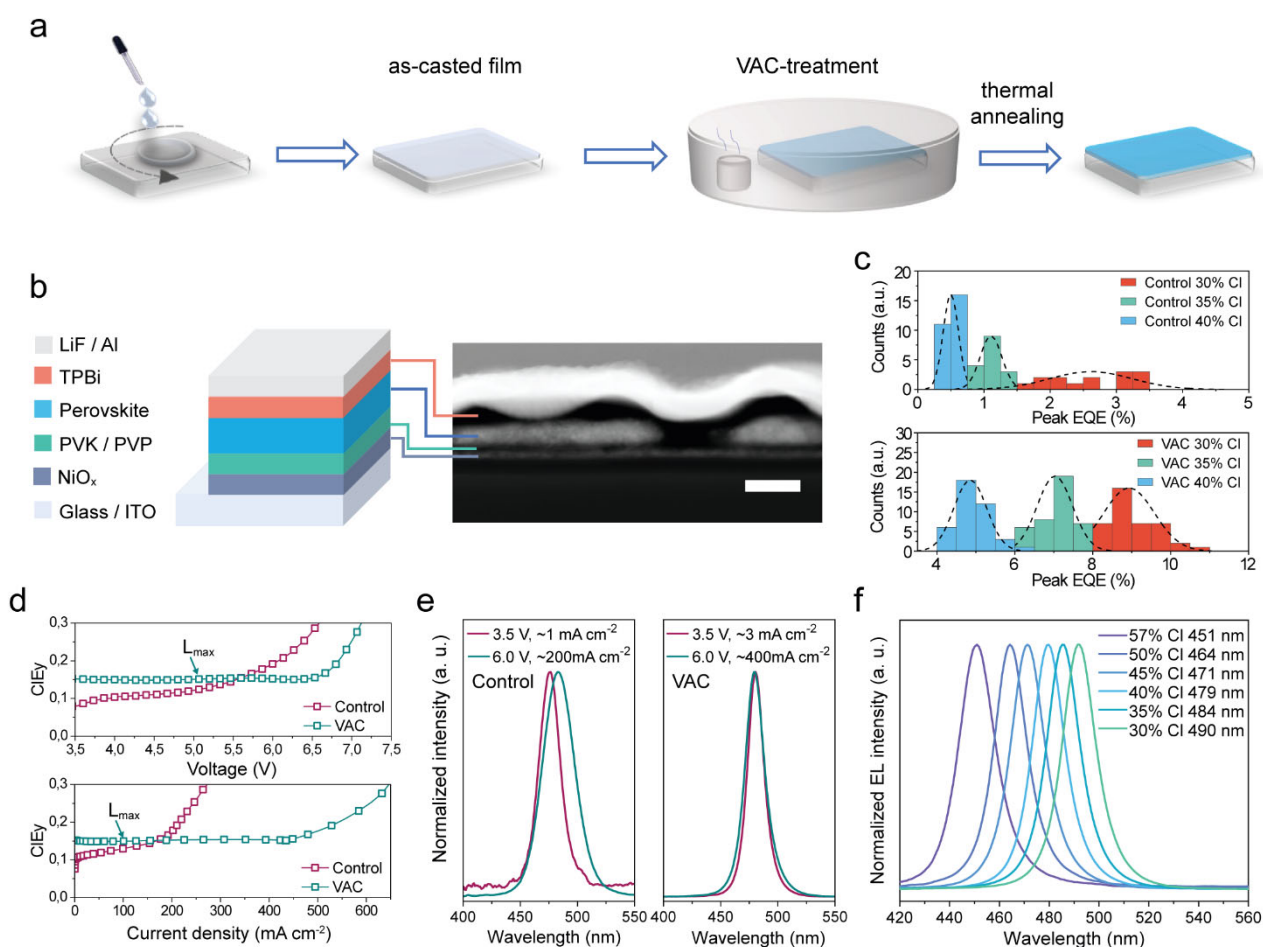
- 362 8. Yuan, S. *et al.* Optimization of low-dimensional components of quasi-2D perovskite films for
363 deep-blue light-emitting diodes. *Adv. Mater.* **31**, 1904319 (2019).
- 364 9. Lu, M. *et al.* Metal halide perovskite light-emitting devices: Promising technology for next-
365 generation displays. *Adv. Funct. Mater.* **29**, 1902008 (2019).
- 366 10. Liu, X. *et al.* Metal halide perovskites for light-emitting diodes. *Nat. Mater.* (2020).
367 <https://doi.org/10.1038/s41563-020-0784-7>.
- 368 11. Liu, Y. *et al.* Efficient blue light-emitting diodes based on quantum-confined bromide perovskite
369 nanostructures. *Nat. Photon.* **13**, 760-764 (2019).
- 370 12. Jiang, Y. *et al.* Spectra stable blue perovskite light-emitting diodes. *Nat. Commun.* **10**, 1868
371 (2019).
- 372 13. Xing, J. *et al.* Color-stable highly luminescent sky-blue perovskite light-emitting diodes. *Nat.*
373 *Commun.* **9**, 3541 (2018).
- 374 14. Dong, Y. *et al.* Bipolar-shell resurfacing for blue leds based on strongly confined perovskite
375 quantum dots. *Nat. Nanotechnol.* **15**, 668-674 (2020).
- 376 15. Protesescu, L. *et al.* Nanocrystals of cesium lead halide perovskites (CsPbX₃, X = Cl, Br, and I):
377 Novel optoelectronic materials showing bright emission with wide color gamut. *Nano Lett.* **15**,
378 3692-3696 (2015).
- 379 16. Li, G. *et al.* Highly efficient perovskite nanocrystal light-emitting diodes enabled by a universal
380 crosslinking method. *Adv. Mater.* **28**, 3528-3534 (2016).
- 381 17. Xiao, Z. *et al.* Mixed-halide perovskites with stabilized bandgaps. *Nano Lett.* **17**, 6863-6869
382 (2017).
- 383 18. Hoke, E. T. *et al.* Reversible photo-induced trap formation in mixed-halide hybrid perovskites for
384 photovoltaics. *Chem. Sci.* **6**, 613-617 (2015).

- 385 19. Nenon, D. P. *et al.* Design principles for trap-free CsPbX₃ nanocrystals: Enumerating and
386 eliminating surface halide vacancies with softer lewis bases. *J. Am. Chem. Soc.* **140**, 17760-17772
387 (2018).
- 388 20. Zheng, X. *et al.* Chlorine vacancy passivation in mixed halide perovskite quantum dots by
389 organic pseudohalides enables efficient Rec. 2020 blue light-emitting diodes. *ACS Energy Lett.* **5**,
390 793-798 (2020).
- 391 21. Li, Z. *et al.* Modulation of recombination zone position for quasi-two-dimensional blue
392 perovskite light-emitting diodes with efficiency exceeding 5%. *Nat. Commun.* **10**, 1027 (2019).
- 393 22. Vashishtha, P., Ng, M., Shivarudraiah, S. B. & Halpert, J. E. High efficiency blue and green
394 light-emitting diodes using ruddlesden–popper inorganic mixed halide perovskites with
395 butylammonium interlayers. *Chem. Mater.* **31**, 83-89 (2018).
- 396 23. Abdi-Jalebi, M. *et al.* Maximizing and stabilizing luminescence from halide perovskites with
397 potassium passivation. *Nature* **555**, 497-501 (2018).
- 398 24. Braly, I. L. *et al.* Hybrid perovskite films approaching the radiative limit with over 90%
399 photoluminescence quantum efficiency. *Nat. Photon.* **12**, 355-361 (2018).
- 400 25. Wang, Q. *et al.* Efficient sky-blue perovskite light-emitting diodes via photoluminescence
401 enhancement. *Nat. Commun.* **10**, 5633 (2019).
- 402 26. Niu, Y. H. *et al.* Thermally crosslinked hole-transporting layers for cascade hole-injection and
403 effective electron-blocking/exciton-confinement in phosphorescent polymer light-emitting diodes.
404 *Appl. Phys. Lett.* **88**, 093505 (2006).
- 405 27. Wright, A. D. *et al.* Electron-phonon coupling in hybrid lead halide perovskites. *Nat. Commun.* **7**,
406 11755 (2016).
- 407 28. Zhao, L. *et al.* Thermal management enables bright and stable perovskite light-emitting diodes.
408 *Adv. Mater.* **32**, 2000752 (2020).

- 409 29. Braly, I. L. *et al.* Current-induced phase segregation in mixed halide hybrid perovskites and its
410 impact on two-terminal tandem solar cell design. *ACS Energy Lett.* **2**, 1841-1847 (2017).
- 411 30. Kuno, M. & Brennan, M. C. What exactly causes light-induced halide segregation in mixed-
412 halide perovskites? *Matter* **2**, 21-23 (2020).
- 413 31. Bischak, C. G. *et al.* Origin of reversible photoinduced phase separation in hybrid perovskites.
414 *Nano Lett.* **17**, 1028-1033 (2017).
- 415 32. Draguta, S. *et al.* Rationalizing the light-induced phase separation of mixed halide organic-
416 inorganic perovskites. *Nat. Commun.* **8**, 200 (2017).
- 417 33. Brennan, M. C., Draguta, S., Kamat, P. V. & Kuno, M. Light-induced anion phase segregation in
418 mixed halide perovskites. *ACS Energy Lett.* **3**, 204-213 (2017).
- 419 34. Barker, A. J. *et al.* Defect-assisted photoinduced halide segregation in mixed-halide perovskite
420 thin films. *ACS Energy Lett.* **2**, 1416-1424 (2017).
- 421 35. Gratia, P. *et al.* Intrinsic halide segregation at nanometer scale determines the high efficiency of
422 mixed cation/mixed halide perovskite solar cells. *J. Am. Chem. Soc.* **138**, 15821-15824 (2016).
- 423 36. Tennyson, E. M., Doherty, T. A. S. & Stranks, S. D. Heterogeneity at multiple length scales in
424 halide perovskite semiconductors. *Nat. Rev. Mater.* **4**, 573-587 (2019).
- 425 37. Brivio, F., Caetano, C. & Walsh, A. Thermodynamic origin of photoinstability in the
426 $\text{CH}_3\text{NH}_3\text{Pb}(\text{I}_{1-x}\text{Br}_x)_3$ hybrid halide perovskite alloy. *J. Phys. Chem. Lett.* **7**, 1083-1087 (2016).
- 427 38. Zhu, C. *et al.* Strain engineering in perovskite solar cells and its impacts on carrier dynamics.
428 *Nat. Commun.* **10**, 815 (2019).
- 429 39. Wang, X. *et al.* Suppressed phase separation of mixed-halide perovskites confined in endotaxial
430 matrices. *Nat. Commun.* **10**, 695 (2019).
- 431 40. Reichert, S. *et al.* Ionic-defect distribution revealed by improved evaluation of deep-level
432 transient spectroscopy on perovskite solar cells. *Phys. Rev. Appl.* **13**, 034018 (2020).

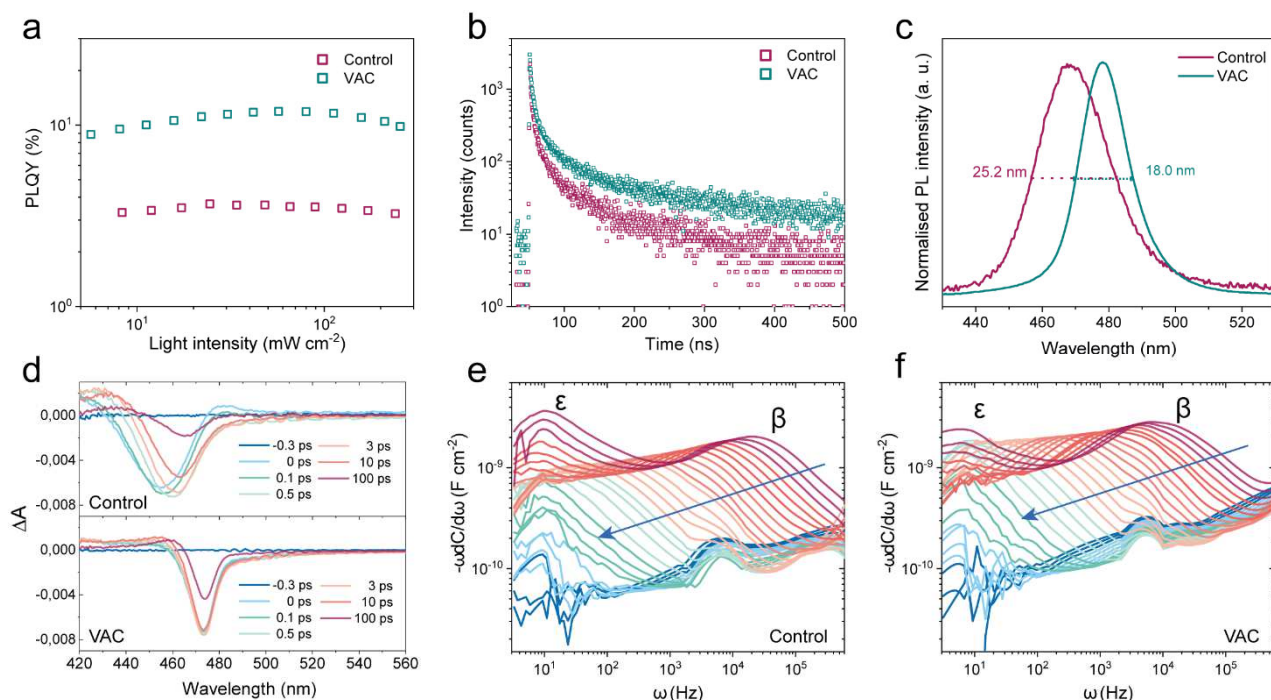
- 433 41. Awni, R. A. *et al.* Influence of charge transport layers on capacitance measured in halide
434 perovskite solar cells. *Joule* **4**, 644-657 (2020).
- 435 42. Doherty, T. A. S. *et al.* Performance-limiting nanoscale trap clusters at grain junctions in halide
436 perovskites. *Nature* **580**, 360-366 (2020).
- 437 43. Jariwala, S. *et al.* Local crystal misorientation influences non-radiative recombination in halide
438 perovskites. *Joule* **3**, 3048-3060 (2019).
- 439 44. Wu, C. *et al.* Improved performance and stability of all-inorganic perovskite light-emitting
440 diodes by antisolvent vapour treatment. *Adv. Funct. Mater.* **27**, 1700338 (2017).
- 441 45. Saliba, M. *et al.* Incorporation of rubidium cations into perovskite solar cells improves
442 photovoltaic performance. *Science* **354**, 206-209 (2016).
- 443 46. Abdi-Jalebi, M. *et al.* Potassium- and rubidium-passivated alloyed perovskite films:
444 Optoelectronic properties and moisture stability. *ACS Energy Lett.* **3**, 2671-2678 (2018).
- 445 47. Zhao, L. *et al.* Redox chemistry dominates the degradation and decomposition of metal halide
446 perovskite optoelectronic devices. *ACS Energy Lett.* **1**, 595-602 (2016).

447



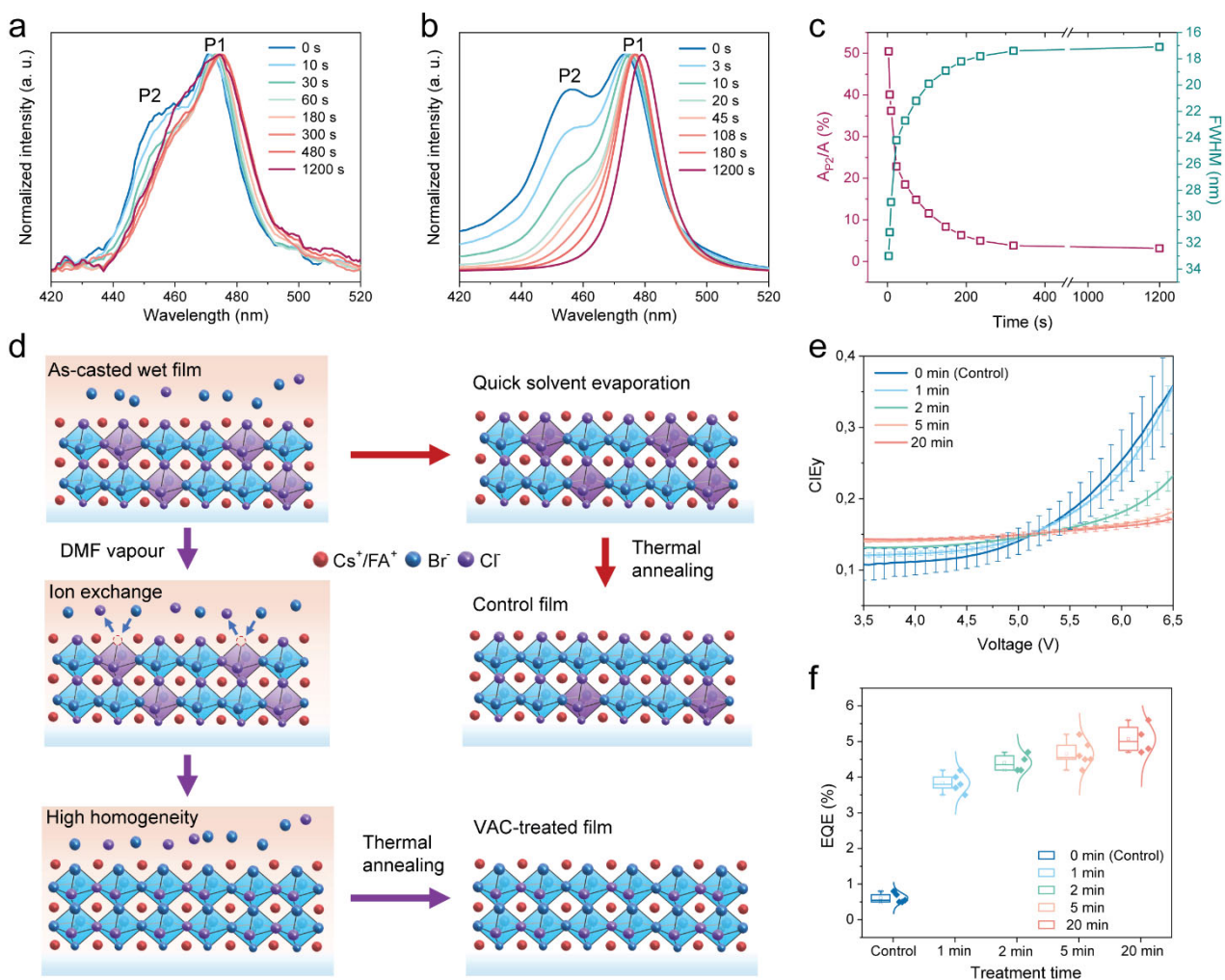
448

449 **Fig. 1 Device fabrication and characteristics.** **a**, An illustration of the VAC-treatment. **b**, Schematic
 450 of the PeLED structure and the HAADF cross-sectional device image. The scale bar is 100 nm. **c**,
 451 Histograms of peak EQEs extracted from control (top) and VAC-treated devices (bottom) with varying
 452 chloride contents (30%, 35%, 40%). **d-f**, Spectral stability for control and VAC-treated devices with
 453 40% Cl loading. The representative plots of CIE_y versus applied voltages (top) and current densities
 454 (bottom) (**d**); EL spectra at low and high voltage/current density for control (left) and VAC-treated
 455 devices (right) (**e**); EL spectra of VAC-treated devices with varying chloride content (30~57%) at
 456 maximum luminance (**f**). The points labelled as L_{max} in Fig. 1d represent the operational condition for
 457 peak luminance.



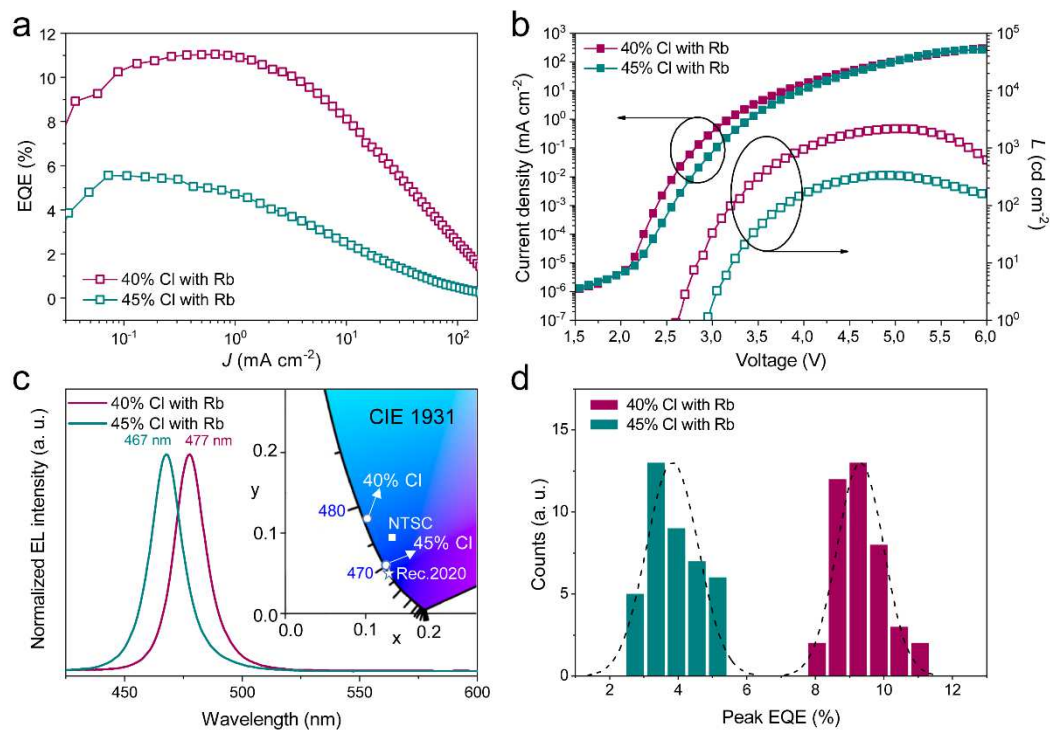
458

459 **Fig. 2 Understanding superior spectral stability of VAC-treated devices.** a-d, Photophysical
 460 characterizations for control and VAC-treated perovskite films: Fluence-dependent PLQYs (a); PL
 461 decay measured by TCSPC (b). PL spectra (c); Transient absorption of control (top) and VAC-treated
 462 films (bottom) after excitation at 400 nm (d). e, f, Derivations of temperature-dependent capacitance
 463 versus frequency plots for control (e) and VAC-treated (f) devices. The blue arrows indicate
 464 temperature change from 350 K to 200 K. Here, two mobile ions marked as β and ϵ are visible.



465

466 **Fig. 3 Understanding the halide redistribution during VAC-process.** **a, b,** PL evolution of the
 467 precursor films kept in the glovebox atmosphere **(a)** and DMF atmosphere **(b)** with time. **c,** the
 468 evolution of emission linewidth and the proportion of P2 (A_{P2}) to the respective total area of the
 469 emission band (A) in VAC-treated films with time. **d,** Schematic illustration of the proposed
 470 mechanism for halide redistribution. Here, the purple $Pb(Br/Cl)_6^{4-}$ octahedra represent chloride-rich
 471 phases in respect to that with stoichiometric bromide/chloride distribution (blue octahedra). The khaki
 472 represents the liquid phase within the films and the blue arrows represent ion exchange process. The
 473 excessive ions within the dried films are not illustrated for clarity. **e, f,** The evolution of CIE
 474 coordinates upon bias **(e)** and peak EQEs of the devices with varying duration of VAC-treatment (0,
 475 1, 2, 5, 20 minutes) **(f)**. The data were extracted from 4 to 6 devices.



476

477 **Fig. 4** The device performance of Rb-passivated perovskites with 40% and 45% Cl contents. **a**,
 478 EQE-current density (J) curves (J -EQE). **b**, Current density-voltage-luminance (J - V - L) characteristics.
 479 **c**, EL spectra and CIE colour coordinates. The square and pentagram in the CIE 1931 (x , y)
 480 chromaticity diagram represent the colour coordinates of primary blue specified in NTSC and
 481 Rec.2020, respectively. **d**, Histograms of the peak EQEs extracted from 40 devices for each case.

482 **Methods**

483 **Materials.** Caesium bromide (CsBr, 99.999%), lead bromide (PbBr₂, 99.999%), lead chloride (PbCl₂,
484 99.999%) was purchased from Alfa Aesar. Formamidinium bromide (FABr) and phenethylammonium
485 bromide (PEABr) were purchased from Greatcell Solar. Rubidium bromide (RbBr, 99.99%),
486 polyvinylpyrrolidone (PVP, average Mw ~55000), 4,7,10-trioxa-1,13-tridecanediamin (TTDDA),
487 poly(9-vinylcarbazole) (PVK, average Mn 25,000~ 50,000) were purchased from Sigma Aldrich. The
488 NiO_x nano-crystals were purchased from Avantama AG and were used without additional treatment.
489 1,3,5-tris(1-phenyl-1H-benzimidazol-2-yl)benzene (TPBi) was purchased from Luminescence
490 Technology corp. Other materials for device fabrication were all purchased from Sigma-Aldrich.

491 **Preparation of the perovskite solution.** Perovskite precursors (CsBr: FABr: PbBr₂: PbCl₂: TTDDA)
492 with a molar ratio of 1.2: 0.3: x: y: 0.1 (where x + y = 1) were mixed and dissolved in dimethyl
493 sulfoxide (DMSO). The precursor concentration as determined by Pb²⁺ is 0.15 M for 30~40% Cl, 0.13
494 M for 45% Cl, 0.11 M for 50% Cl, and 0.09 M for 57% Cl, respectively. The precursor solutions were
495 stirred at 80°C for 4h before use. For the low-dimensional perovskites, precursors (PEABr: CsBr PbBr₂:
496 PbCl₂) with a molar ratio of 0.9:1.1:0.4:0.6 mixed and dissolved in DMSO to make a solution with 30%
497 Cl-content. The precursor concentration determined by Pb²⁺ is 0.15 M.

498 **PeLED fabrication.** Glass substrates with patterned Indium tin oxide (ITO) were sequentially cleaned
499 by detergent and TL-1 (a mixture of water, ammonia (25%) and hydrogen peroxide (28%) (5:1:1 by
500 volume)). The clean substrates were then treated by ultraviolet-ozone for 10 min. NiO_x was spin-coated
501 in air at 4,000 r.p.m. for 30 s, followed by baking at 150 °C for 10 min in air. The substrates were then
502 transferred into a nitrogen-filled glovebox (< 0.1 ppm H₂O, < 0.1 ppm O₂). PVK (4 mg ml⁻¹ in
503 chlorobenzene) was deposited at 3000 r.p.m. followed by thermal annealing at 150°C for 10 min. Next,

504 a thin layer of PVP (2.0 mg mL^{-1} in isopropyl alcohol (IPA)) was deposited at 3000 r.p.m. and baked
505 at 100°C for 5 min. After cooling down to room temperature, the perovskite solutions with varying
506 bromide/chloride ratios were deposited at 3000 r.p.m. Directly after spin-coating, the films were put
507 in an unsealed $\varnothing 60$ mm petri-dish (with lid) at room temperature, where 20 μl of dimethylformamide
508 had been dropped 10 min prior to the film placement. After 20 min of vapour assisted crystallisation
509 (VAC) treatment, the films were annealed at 80°C for 8 min. For low-dimensional perovskite films
510 with mixed halides, the treatment duration is 10 min and the annealing condition is 80°C for 5 min.
511 Finally, the electron transport layer TPBi and top contacts LiF/Al (1 nm / 100 nm) were deposited by
512 thermal evaporation through shadow masks at a base pressure of $\sim 10^{-7}$ torr. The device area was 7.25
513 mm^2 .

514 **PeLED characterization.** All PeLED device characterizations were performed at room temperature
515 in a nitrogen-filled glovebox without encapsulation. A Keithley 2400 source-meter and a fibre
516 integration sphere (FOIS-1) coupled with a QE Pro spectrometer (Ocean Optics) were utilized. The
517 absolute radiance was calibrated by a standard Vis–NIR light source (HL-3P-INT-CAL plus, Ocean
518 Optics). The PeLED devices were measured on top of the integration sphere and only forward light
519 emission can be collected. The devices were swept from zero bias to forward bias with a step voltage
520 of 0.05 V, lasting for 100 ms at each voltage step for stabilisation. The sweep duration from 1 to 7 V
521 is 70 seconds (with a scan rate of 86 mV S^{-1}). The EQE and spectral evolution with time was measured
522 using the same system.

523 **Perovskite film characterization.** Top-view scanning electron microscope (SEM) images were tested
524 by LEO 1550 Gemini. Steady-state PL spectra of the perovskite films were recorded by a fluorescent
525 spectrophotometer (F-4600, HITACHI) with a 200 W Xe lamp as an excitation source. UV-Vis

526 absorbance spectra were collected using a PerkinElmer model Lambda 900. X-ray diffraction patterns
527 were measured using a Panalytical X'Pert Pro with an X-ray tube (Cu K α , $\lambda = 1.5406 \text{ \AA}$).

528 X-ray photoelectron spectroscopy (XPS) tests were performed by a Scienta ESCA 200
529 spectrometer in ultrahigh vacuum ($\sim 1 \times 10^{-10}$ mbar) with a monochromatic Al (K α) X-ray source
530 providing photons with 1,486.6 eV. The experimental was set so that the full-width at half-maximum
531 of clean Au 4f 7/2 line (at the binding energy of 84.00 eV) was 0.65 eV. All spectra were characterized
532 at a photoelectron take-off angle of 0°. Ultraviolet photoelectron spectroscopy (UPS) was carried out
533 using a Kratos AXIS Supra on perovskite samples spun-cast on ITO/NiO $_x$ /PVK/PVP. He I (21.22eV)
534 radiation was generated from a helium discharge lamp. Samples were biased at 9.1V.

535 In-situ PL of the crystallisation process was collected using the integrating sphere and the QE Pro
536 spectrometer as described above, and a 365 nm UV laser as excitation source. In-situ transmittance
537 tests were performed using the same spectrometer but with a solar simulator (AM 1.5G) as the light
538 source. A ND filter was used to decrease the light intensity. The systems were illustrated in
539 Supplementary Fig. 21.

540 Time-correlated single photon counting (TCSPC) measurements were carried out by using an
541 Edinburgh Instruments FL1000 with a 405 nm pulsed picosecond laser (EPL-405). Fluence dependent
542 PLQY was measured using a 405 nm continuous wave laser, an integrating sphere and the same
543 spectrometer. The perovskite films were deposited on ITO/NiO $_x$ /PVK/PVP substrates under identical
544 conditions as for the PeLEDs, and encapsulated using glass slides and UV-curable resin.

545 Grazing-incidence wide-angle X-ray scattering (GIWAXS) was recorded in Shanghai
546 Synchrotron Radiation Facility. The diffraction patterns were collected by two dimensional MarCCD
547 225 detector with 234 mm from samples to the detector. All the samples were protected with N $_2$ gas

548 during the measurements. To assure the diffraction intensity, an exposure time of 15 s was adopted
549 with an incidence angle of 0.5° , and the wavelength of the X-ray was 1.24 \AA (10 KeV). For all these
550 tests, the perovskite films were deposited on ITO/NiO_x/PVK/PVP substrates under identical conditions
551 as device fabrication.

552 **Scanning transmission electron microscopy (STEM) and Energy-dispersive X-ray spectroscopy**
553 **(EDX).** The STEM samples were fabricated by using the FEI Focused Ion Beam (FIB) system (Helios
554 Nanolab 600i). A FEI Titan-G2 Cs-corrected transmission electron microscope with 300 KV
555 accelerating voltage was used to get the high angle angular dark field (HAADF) images of the samples.
556 The STEM elemental mapping images were collected by four silicon drift windowless detectors
557 (Super-EDX) in the FEI Titan-G2 Cs-corrected transmission electron microscope. The energy
558 resolution of the Super-EDX was 137 eV.

559 **Transient absorption.** A femtosecond oscillator (Mai Tai, Spectra Physics) is used as a seed laser for
560 a regenerative amplifier (Spitfire XP Pro, Spectra Physics) which generates well collimated beam of
561 femtosecond pulses (800 nm, 80 fs pulse duration, 1 kHz repetition rate). The second harmonic
562 generated by a BBO crystal was used as pump (400 nm). White light continuum (WLC) as the probe
563 was produced by focusing the 800 nm fs pulse on a thin CaF₂ plate. Polarization between the pump
564 and probe was set to the magic angle (54.7°). Both pump and probe pulses are monitored to compensate
565 for the laser fluctuations during the measurements.

566 **Admittance spectroscopy.** For the defect studies we used a setup consisting of a Zurich Instruments
567 MFLI lock-in amplifier with MF-IA and MF-MD options, a Keysight Technologies 33600A function
568 generator and a cryo probe station Janis ST500 with a Lakeshore 336 temperature controller. For
569 determining the ion signature using admittance spectroscopy we varied the sample temperature from

570 200 K to 350 K in 5 K steps, controlled accurately within 0.01 K and using liquid nitrogen for cooling.
 571 The capacitance in term of a C||R equivalence model was measured by applying an ac voltage with
 572 amplitude of $V_{ac} = 20$ mV and varying the frequency from 0.6 Hz to 3.2 MHz. The rates e_t are obtained
 573 from the peak maxima of the derivative of the capacitance. These rates are linked to the diffusion
 574 coefficient D in terms of the underlying hopping process of the mobile ions^{48,49},

$$575 \quad e_t = \frac{e^2 N_{eff} D}{k_B T \epsilon_0 \epsilon_R},$$

576 (1)

577 where N_{eff} refers to the effective doping density, e is the elementary charge, k_B is the Boltzmann
 578 constant, T the temperature, ϵ_0 the dielectric constant and ϵ_R the relative permittivity. For the
 579 calculation of D_{300K} we used a dielectric permittivity of 19.2⁵⁰. Since ion migration is a thermally
 580 activated process, the diffusion coefficient depends on the temperature,

$$581 \quad D = D_0 \exp\left(-\frac{E_A}{k_B T}\right)$$

582 (2)

583 with the activation energy for ion migration E_A and the diffusion coefficient at infinite temperatures
 584 D_0 . Subsequently, E_A and D_0 can be extracted from the slope and the cross section with the emission
 585 rate axis using Eqns. (1) and (2). By taking into account the surface polarization caused by the
 586 accumulation of mobile ions at the interfaces of the perovskite layer, the ion concentration N_i is
 587 determined as⁵¹,

$$588 \quad N_i = \frac{k_B T \Delta C^2}{e^2 \epsilon_0 \epsilon_R}$$

589 (3)

590 Here, ΔC refers to the capacitance step in the admittance spectra of the contributing ions.

591 **Reference**

- 592 48. Heiser, T. & Mesli, A. Determination of the copper diffusion coefficient in silicon from transient
593 ion-drift. *Appl. Phys. A* **57**, 325-328 (1993).
- 594 49. Futscher, M. H. *et al.* Quantification of ion migration in CH₃NH₃PbI₃ perovskite solar cells by
595 transient capacitance measurements. *Mater. Horiz.* **6**, 1497-1503 (2019).
- 596 50. Schlaus, A. P. *et al.* How lasing happens in CsPbBr₃ perovskite nanowires. *Nat. Commun.* **10**,
597 265 (2019).
- 598 51. Almora, O. *et al.* Capacitive dark currents, hysteresis, and electrode polarization in lead halide
599 perovskite solar cells. *J. Phys. Chem. Lett.* **6**, 1645-1652 (2015).

Figures

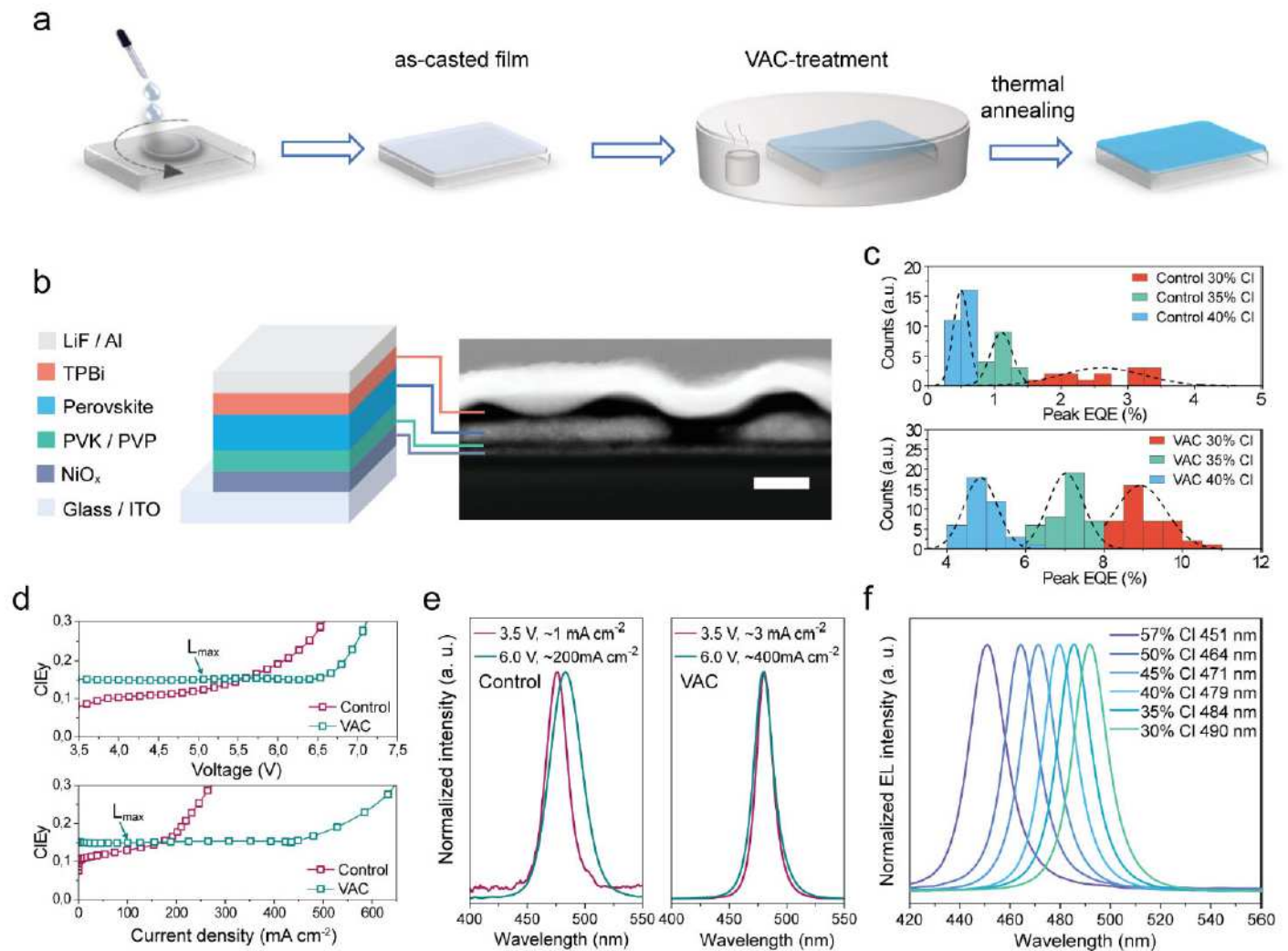


Figure 1

Device fabrication and characteristics. a, An illustration of the VAC-treatment. b, Schematic of the PeLED structure and the HAADF cross-sectional device image. The scale bar is 100 nm. c, Histograms of peak EQEs extracted from control (top) and VAC-treated devices (bottom) with varying chloride contents (30%, 35%, 40%). d-f, Spectral stability for control and VAC-treated devices with 40% Cl loading. The representative plots of CIEy versus applied voltages (top) and current densities (bottom) (d); EL spectra at low and high voltage/current density for control (left) and VAC-treated devices (right) (e); EL spectra of VAC-treated devices with varying chloride content (30~57%) at maximum luminance (f). The points labelled as L_{max} in Fig. 1d represent the operational condition for peak luminance.

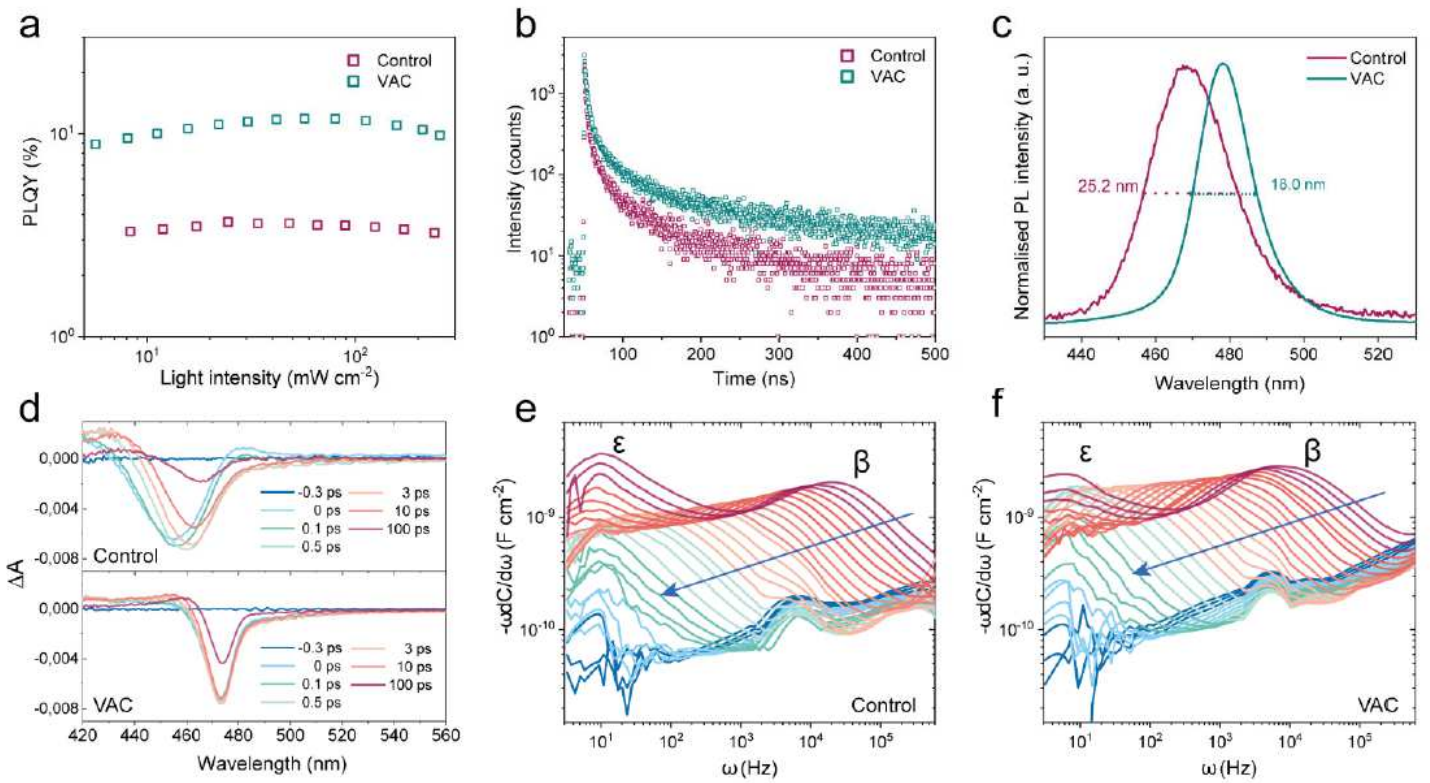


Figure 2

Understanding superior spectral stability of VAC-treated devices. a-d, Photophysical characterizations for control and VAC-treated perovskite films: Fluence-dependent PLQYs (a); PL decay measured by TCSPC (b). PL spectra (c); Transient absorption of control (top) and VAC-treated films (bottom) after excitation at 400 nm (d). e, f, Derivatives of temperature-dependent capacitance versus frequency plots for control (e) and VAC-treated (f) devices. The blue arrows indicate temperature change from 350 K to 200 K. Here, two mobile ions marked as β and ϵ are visible.

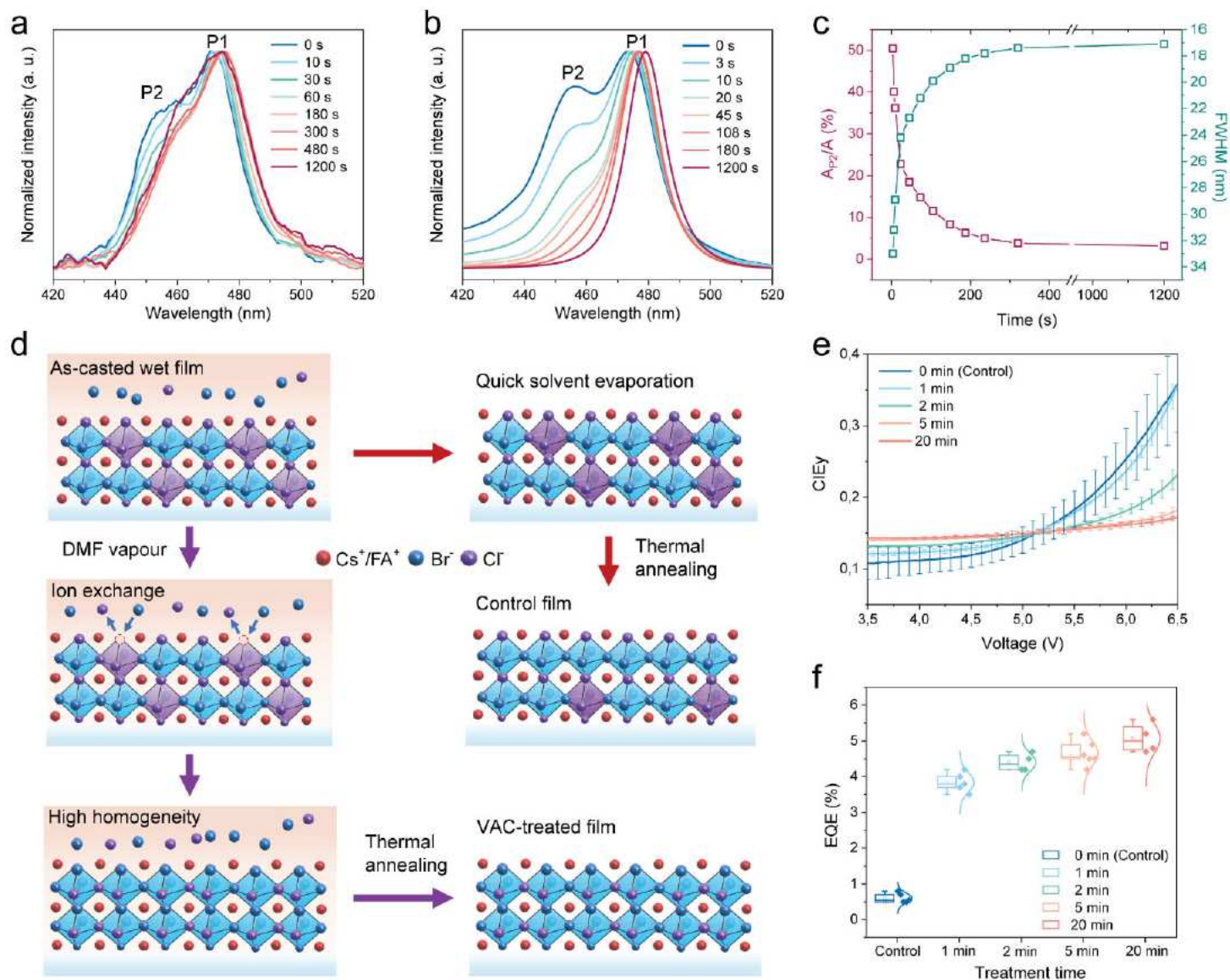


Figure 3

Understanding the halide redistribution during VAC-process. a, b, PL evolution of the precursor films kept in the glovebox atmosphere (a) and DMF atmosphere (b) with time. c, the evolution of emission linewidth and the proportion of P2 (A_{P2}) to the respective total area of the emission band (A) in VAC-treated films with time. d, Schematic illustration of the proposed mechanism for halide redistribution. Here, the purple $Pb(Br/Cl)_6$ -octahedra represent chloride-rich phases in respect to that with stoichiometric bromide/chloride distribution (blue octahedra). The khaki represents the liquid phase within the films and the blue arrows represent ion exchange process. The excessive ions within the dried films are not illustrated for clarity. e, f, The evolution of CIE coordinates upon bias (e) and peak EQEs of the devices with varying duration of VAC-treatment (0, 1, 2, 5, 20 minutes) (f). The data were extracted from 4 to 6 devices.

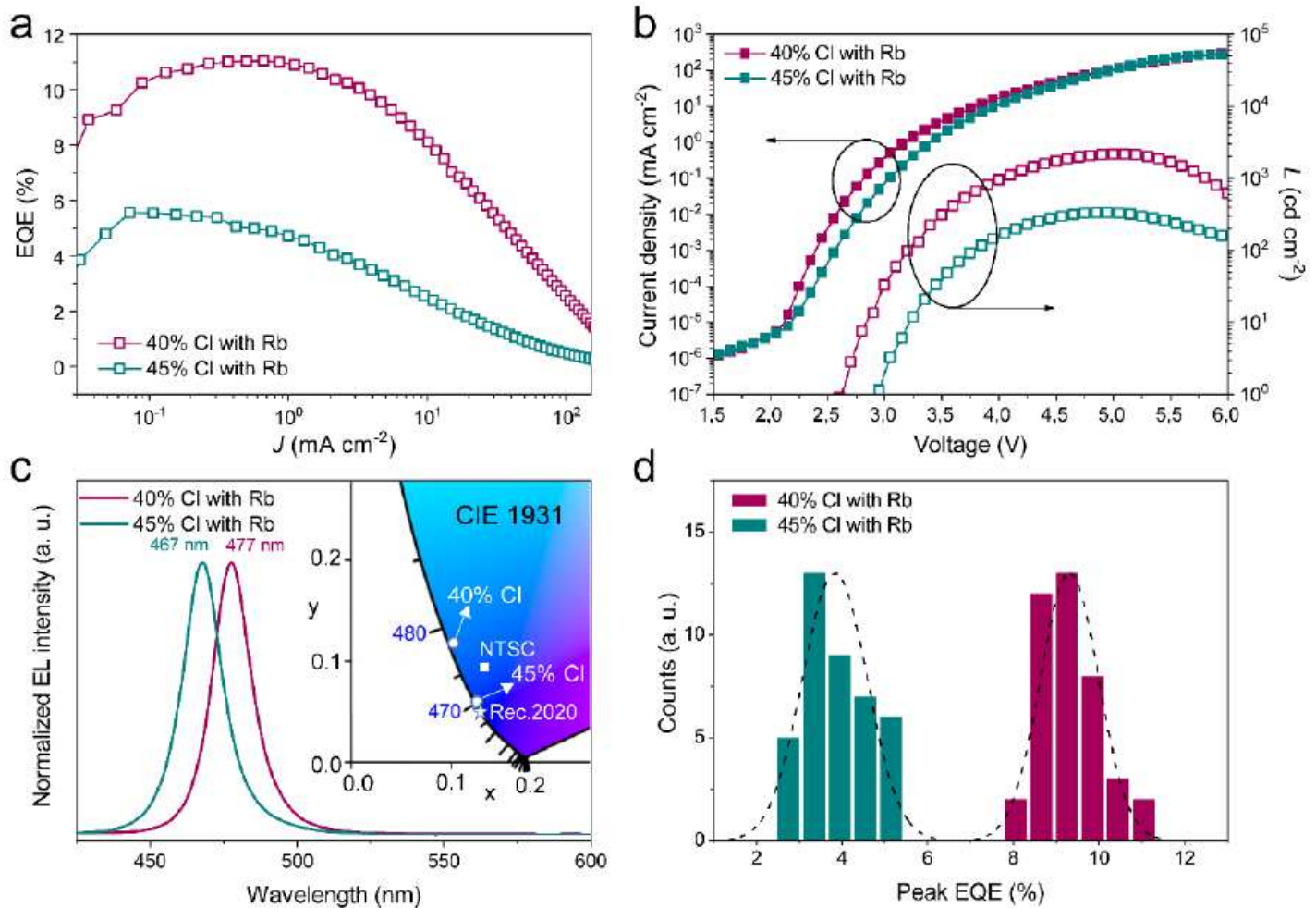


Figure 4

The device performance of Rb-passivated perovskites with 40% and 45% Cl contents. a, EQE-current density (J) curves (J-EQE). b, Current density-voltage-luminance (J-V-L) characteristics. c, EL spectra and CIE colour coordinates. The square and pentagram in the CIE 1931 (x , y) chromaticity diagram represent the colour coordinates of primary blue specified in NTSC and Rec.2020, respectively. d, Histograms of the peak EQEs extracted from 40 devices for each case.

Supplementary Files

This is a list of supplementary files associated with this preprint. Click to download.

- [SIJrevision10.14.pdf](#)